Shaping 90 wt% NanoMOFs into Robust Multifunctional Aerogels Using Tailored Bio-Based Nanofibrils

(Article begins on next page)

23 April 2024

RESEARCH ARTICLE

Shaping 90 wt% NanoMOFs into Robust Multifunctional Aerogels Using Tailored Bio-Based Nanofibrils

Jowan Rostami,* Tobias Benselfelt, Lorenza Maddalena, Civan Avci, Farhiya Alex Sellman, Goksu Cinar Ciftci, Per A. Larsson, Federico Carosio, Farid Akhtar, Weiqian Tian,* and Lars Wågberg*

Metal–organic frameworks (MOFs) are hybrid porous crystalline networks with tunable chemical and structural properties. However, their excellent potential is limited in practical applications by their hard-to-shape powder form, making it challenging to assemble MOFs into macroscopic composites with mechanical integrity. While a binder matrix enables hybrid materials, such materials have a limited MOF content and thus limited functionality. To overcome this challenge, nanoMOFs are combined with tailored same-charge high-aspect-ratio cellulose nanofibrils (CNFs) to manufacture robust, wet-stable, and multifunctional MOF-based aerogels with 90 wt% nanoMOF loading. The porous aerogel architectures show excellent potential for practical applications such as efficient water purification, CO_2 and CH_4 gas adsorption and separation, and fire-safe insulation. Moreover, a one-step carbonization process enables these aerogels as effective structural energy-storage electrodes. This work exhibits the unique ability of high-aspect-ratio CNFs to bind large amounts of nanoMOFs in structured materials with outstanding mechanical integrity—a quality that is preserved even after carbonization. The demonstrated process is simple and fully discloses the intrinsic potential of the nanoMOFs, resulting in synergetic properties not found in the components alone, thus paving the way for MOFs in macroscopic multifunctional composites.

1. Introduction

Metal–organic frameworks (MOFs) have emerged as one of the leading forms of synthetic crystalline networks. MOFs can achieve energy-efficient and atom-economical self-assembly,[1] and their diversity provides a versatile toolbox with chemical and structural precision for tailoring materials toward different functionalities.[2,3] The key is to utilize the MOFs' unique and tunable interior pore environment, with an ultrahigh porosity that entails large specific surface areas.[3] However, common MOFs are typically collected as powders, which are highly impractical in most applications.[4] In the pursuit of a coherent MOF-material, metal–organic aerogels (MOAs), i.e., aerogels made from MOFs with chemically crosslinked matrices, have been proposed.[5] However, the fabrication of MOAs is challenging since MOFs lack the propensity to form stable networks of sufficient structural

J. Rostami, T. Benselfelt, F. A. Sellman, G. Cinar Ciftci, P. A. Larsson,
W. Tian, L. Wågberg
Department of Fibre and Polymer Technology
Division of Fibre Technology
KTH Royal Institute of Technology
Stockholm 11428, Sweden
E-mail: jowan@kth.se; tianweiqian@ouc.edu.cn; wagberg@kth.se
T. Benselfelt
School of Materials Science and Engineering
Nanyang Technological University
Singapore 639798, Singapore
L. Maddalena, F. Carosio
Dipartimento di Scienza Applicata e Tecnologia
Politecnico di Torino-Alessandria Campus
Viale Teresa Michel 5, Alessandria 15121, Italy

C. Avci
Sorbonne Université
CNRS
Laboratoire de Chimie de la Matière Condensée de Paris (LCMCP)
Paris F-75005, France
F. A. Sellman, L. Wågberg
Department of Fibre and Polymer Technology
Wallenberg Wood Science Center (WWSC)
KTH Royal Institute of Technology
Stockholm 11428, Sweden
G. Cinar Ciftci
Material and Surface Design
RISE Research Institutes of Sweden
Stockholm 11486, Sweden
F. Akhtar
Division of Materials Science
Luleå University of Technology
Luleå 97187, Sweden
W. Tian
School of Materials Science and Engineering
Ocean University of China
Qingdao, Shandong 266100, China

integrity.[6] In this respect, crystallization and precipitation of the MOF components during the aerogel processing severely limits the development and use of pure MOAs in practical applications.[7]

One way to facilitate their utilization is to shape MOFs into easy-to-handle objects by incorporating them into a solid host matrix. Ideally, the host matrix should be a lightweight, highly porous, and physically strong material, such as an aerogel, which provides accessibility to the internal pore structure of the MOFs and sufficient mechanical robustness.[8–10] The development of state-of-the-art MOF-containing hybrid aerogels has resulted in many possible applications such as adsorption and separation of gases, energy storage, purification, catalysis, and molecular recognition.[11,12] These aerogels are composed of MOFs that provide the functionality and (bio)polymers or high-aspect-ratio particles that provide a continuous network of sufficient mechanical strength.[13] Among these network-providing polymers, cellulosic nanomaterials have emerged as an exciting, bio-based option, providing both in situ and ex situ functionalization with MOFs to form hybrid aerogels.[8,13,14] However, the relatively high fibril/polymer content needed for such materials hinders the full functionality and possible application of the MOFs.[15] Therefore, the development of mechanically robust aerogels with a maximum MOF loading and minimal polymeric content is crucial in reaching the full application potential of these systems.[8,12,16]

In this work, we present a versatile strategy to prepare aerogels with 90 wt% nanoMOF loading, using only 10 wt% high-aspect-ratio cationic cellulose nanofibrils (CNFs) as efficient nanosized building blocks that enable a strong interfacial adhesion in synergistically interconnected networks. This strategy provides a simple, water-based preparation procedure, which results in anisotropically ordered, mechanically robust, and wet-stable MOF aerogels. The resulting aerogels allow the intrinsic properties of the MOFs to be fully utilized, as demonstrated by their excellent ability to physisorb gases and purify water. Interestingly, this combination of a network of mechanically robust and flexible CNFs and high specific-surface-area nanoMOFs shows synergistic properties not found in any of the components alone, such as excellent flame retardancy. The aerogels were also carbonized in an inert atmosphere, forming compressible and elastic N-doped carbon aerogels that can be used as supercapacitor electrodes. The preparation of these aerogels and their carbonization demonstrate a precise, efficient, and sustainable method to obtain high-value-added multifunctional materials, which show unique properties useful for various applications. Their flame retardancy, controlled nanopore structure, and gas-separation/adsorption properties make them ideal as high-value-added insulation materials in extreme environments. Their high specific surface area, low weight, and excellent conductivity make them ideal as sustainable supercapacitor electrodes.

2. Results and Discussion

To overcome the challenges of a lack of shapeability and mechanical integrity in powdered MOFs, we have developed self-supporting and mechanically resilient nanoMOF-rich aerogels.

Zeolitic imidazolate framework-8 (ZIF-8) was chosen as a model MOF system. Cationic nanoMOFs were mixed with a small fraction (10 wt%) of very high-aspect-ratio, cationic CNFs to obtain an overall cationic hybrid gel. The hybrid gel was freeze-cast and lyophilized to obtain anisotropically ordered MOF-based aerogels suitable for different advanced applications.

ZIF-8 MOFs were synthesized in aqueous media by coordinating 2-methylimidazole (2-MiM) and Zn^{2+} ions in tetrahedral conformation, generating micrometer-sized particles with a sodalite topology that shows relatively rapid sedimentation (**Figure 1**a,b and Figure S1, Supporting Information). However, the addition of the cationic surfactant cetrimonium bromide (CTAB) inhibits crystal growth and stabilizes the particles,[17] resulting in cationic nanoZIF-8 (nZIF-8) particles with excellent colloidal stability. The nanoMOFs have an average size of 178 ± 22 nm (Figure 1a,c and Figure S1, Supporting Information), a ζ-potential of 37 ± 1 mV (0.1 wt%, pH $\approx$ 9), and a surface charge density of 26 ± 2 μmol g^{-1}. We combined these nZIF-8 particles with a small amount (10 wt%) of colloidally stable, wood-derived, cationic CNFs with widths of 0.5–3.2 nm, lengths of up to 3.6 μm, a ζ-potential of 131 ± 4 mV (0.1 wt%, pH $\approx$ 7), and a surface charge density of 613 ± 26 μmol g^{-1} (Figure 1d,e, and Figure S2, Supporting Information).

First, we used quartz crystal microbalance measurements to clarify the interactions between the nZIF-8 and the CNFs (Figure S3, Supporting Information). The measurements showed an association between nZIF-8 and the CNFs, thus establishing that an interaction occurs between the two same-charge nanoparticles in the wet state. This finding might be counterintuitive, since both are positively charged. However, the nZIF-8 particles have a very low charge and are desorbed upon extended rinsing, indicating the weak and non-ionic nature of the interaction. Therefore, the dominating attractive force behind the initial adsorption of the nanoMOFs at the cellulose/water interface is probably van der Waals interactions, which rapidly increase in strength as the two types of nanoparticles are pushed closer together by the growth of ice crystals during freeze casting. Due to the same sign of the charge of the particles, macroscopic flocculation between the nanoparticles can be avoided (Figure S4, Supporting Information), which is essential in order to preserve the inherent properties of the two materials.

Second, the high-aspect-ratio CNFs constitute the basis for forming a highly entangled gel network at very low concentrations, with long-range stress transfer preventing stress accumulation in the more brittle contacts between the nanoMOFs. The aspect ratio of the cationic CNFs ($l/w \approx 870$) in this work is significantly higher than the more commonly reported values for typical anionically charged wood-derived CNFs ($l/w \approx 200$).[18,19] This is mainly because our modification procedure preserves the length of the fibrils, resulting in a critical overlap concentration—that is, the threshold concentration at which the moving fibrils start to interfere with each other—of 3 μg mL^{-1} (Tables S1 and S2, Supporting Information). This concentration is significantly lower in comparison with values for anionically charged wood-derived CNFs ($\approx$50 μg mL^{-1}).[19] Furthermore, the final concentration of 0.25 wt% CNFs in our wet gel mixtures results in a crowding factor—that is, the number of fibrils occupying the rotational volume of a fibril—of 845 (Tables S1
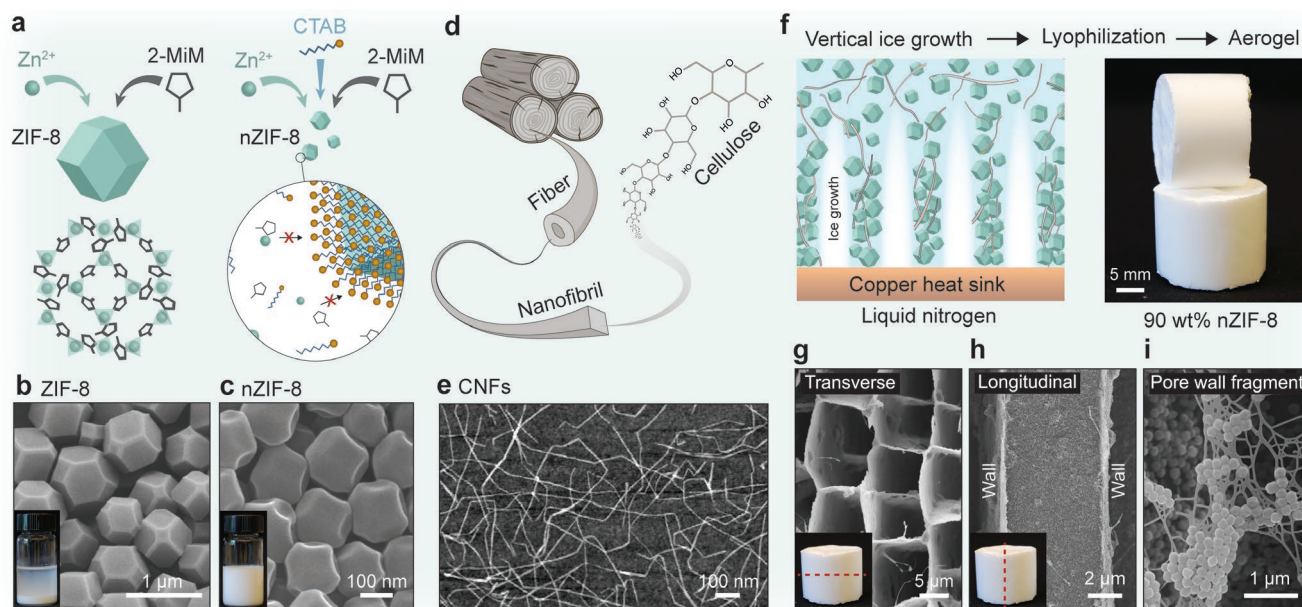
Figure 1. Fabrication and microstructure of nanoMOF aerogels. a) Schematic illustration of the formation of zeolitic imidazolate framework-8 (ZIF-8) particles via self-assembly of 2-methylimidazole (2-MiM) linkers and tetrahedrally coordinated Zn^{2+} ions, with and without the use of cetrimonium bromide (CTAB) for nanoMOF stabilization. b) Representative scanning electron microscopy (SEM) image of micrometer-sized ZIF-8 particles formed without CTAB; the inset shows the partial sedimentation of the dispersion after 2 h. c) Representative SEM image of nanoZIF-8 (nZIF-8) particles formed with CTAB; the inset shows a stable dispersion with no sedimentation after 2 h. d) Schematic image of the hierarchical structure of wood: from timber, via fibers, to nanofibrils and cellulose polymer chains. e) Representative atomic force microscopy image of the cationic cellulose nanofibrils (CNFs). f) Illustration of the formation mechanism of anisotropically frozen hydrogels and a representative photograph of the aerogels, composed of 90 wt% nZIF-8 and 10 wt% CNFs, achieved by lyophilization. g,h) SEM images of the aerogels imaged in the transverse (g) and longitudinal (h) direction. i) High-magnification SEM image of a porous part of the pore wall shown in (h).

and S2, Supporting Information), indicating that there are many contact points for these extremely high-aspect-ratio fibrils. The number of contacts naturally increases further upon water removal, creating a fine but stiff mesh that holds the nanoMOFs in place, as shown in Figure 1i. In turn, the higher surface-to-volume ratio of the nanoMOFs enables the formation of stable homogeneous mixtures and an increased number of CNF contacts in the dried state.

The CNF/nanoMOF gel mixtures were then freeze-cast and lyophilized to obtain highly porous nZIF-8–CNF aerogels (AG^{nZIF-8}) with parallel tubular pores and pore walls covered with nZIF-8 particles (Figure 1f–i and Figure S5, Supporting Information). The obtained microporous and mesoporous aerogel (97% porosity) (Table S3, Supporting Information) is self-supporting, with a specific surface area of 1470 m^2 g^{-1}—that is, about 90% of that of the neat nZIF-8 MOFs (1610 m^2 g^{-1}) (Figures S6–S9 and Table S4, Supporting Information). The obtained surface area of the nZIF-8 MOFs also indicates that CTAB is sufficiently removed and is not blocking the pores, as the specific surface area results agree with literature values and are not affected by the CTAB.[17]

MOF-based aerogels with high loadings are generally weak, and the ability to create a strong material in the direction of the applied stress is vital in many practical applications. The unidirectional freeze-casting demonstrates the possibility of focusing the strength and stiffness of the aerogel in the pore direction while adding flexibility in the transverse direction. The anisotropy also provides a distinct pore direction that allows a guided flow of heat, liquid, or gas through the MOF-containing network without building too-high stress that compresses the aerogel. Therefore, a tailored aerogel anisotropy can be beneficial for obtaining characteristics such as flame retardancy or applications such as filtration or gas adsorption and separation.[21,22]

To demonstrate the efficiency of the aerogel networks with an average density of only 29.3 ± 0.5 kg m^{-3}, we measured their mechanical properties under compression (Table S5, Supporting Information). The compression curves have the classical shape of a porous material: a linear elastic region followed by yielding as the pore walls collapse, and after that a plateau region with compression of pores before increasing pressure by densification.[23] The longitudinal compression (**Figure 2**a)— that is, the compression in the pore direction—resulted in an average specific compressive modulus of 35.6 ± 2.9 kPa m^3 kg^{-1}. This stiffness can be attributed to the high modulus of both the nanoMOFs and CNFs.[24] After compression to 90% of the original size, the specific surface area (1460 m^2 g^{-1}) was not different from that of the non-compressed aerogel (1470 m^2 g^{-1}) (Figure S10 and Table S6, Supporting Information). This result demonstrates that, through compression, the bulk density of the aerogel can be controlled for applications that require a denser material without compromising the desired high specific surface area of the nanoMOFs present in the aerogels.

The specific compressive modulus in the transverse direction—perpendicular to the pores—was 1.5 ± 0.3 kPa m^3 kg^{-1} (Figure 2b). These mechanical properties are among the best-reported values for MOF-containing aerogels, especially since the MOF loading is the highest reported to date (Figure 2c),
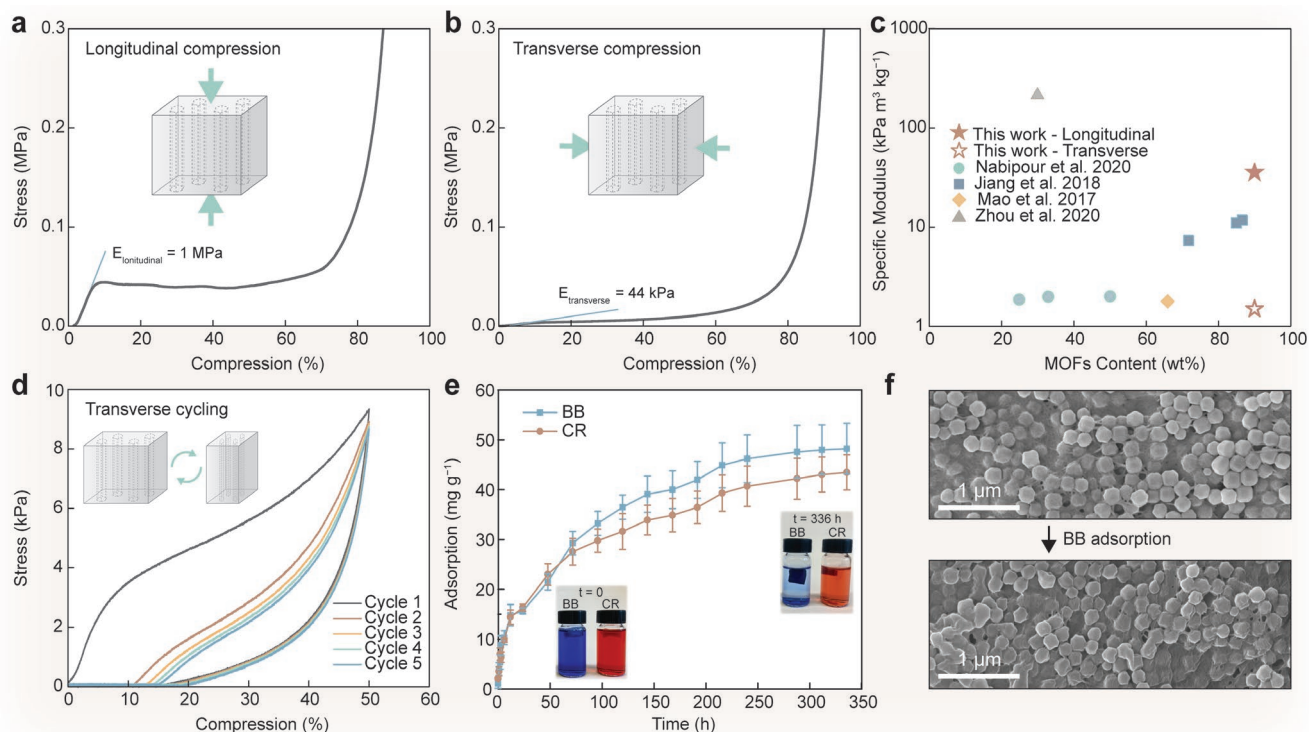
Figure 2. Mechanical properties of the MOF-based aerogels and adsorption capacity of anionic dyes. a,b) Compressive stress–strain curves for AG^{nZIF-8}, compressed in the longitudinal (a) and transverse (b) directions of the ice growth during freeze casting. c) Specific modulus of aerogels as a function of MOF content; data from our study and the literature.[9,20] d) Cyclic compressions (five cycles) to 50% compression of the original size of an AG^{nZIF-8}. e) Dye adsorption capacity of AG^{nZIF-8} aerogels in 0.05 mg g^{-1} dye solutions of brilliant blue (BB) and Congo red (CR) at pH 7.4, with photographs taken immediately after submersion and after 336 h. f) SEM image of the MOF-covered aerogel pore walls, before and after 366 h of BB sorption, showing the intact microstructure of the MOFs after dye adsorption.

to the best knowledge of the authors.[9,20] The cyclic mechanical stability of the dry aerogels in the transverse direction (Figure 2d) shows that the pores can indeed recover when the stress is released. The resulting shape recovery was 70% for the first cycle, followed by 86%, 86%, 83%, and 84% for the consecutive cycles. Thus, the material was slightly permanently damaged during the first cycle, indicating that buckling of the pore walls upon loading without fracturing, enabling a partial recovery and a cyclability similar to that of sponges.[25]

Improved wet stability is also required for use under wet conditions. Although the aerogels are made of two cationic constituents, nZIF-8 and CNFs, without the addition of crosslinkers or multivalent ions, wet stability can be obtained simply by utilizing the irreversible association of CNFs under mild heat treatment, also known as the hornification of cellulose-rich materials.[26] Heat-treating a dry film of pure CNFs (i.e., a nanopaper) at 120 °C for a specific time results in a reduced swelling that is proportional to the heating time (Figure S11, Supporting Information). Following the same principle, heat-treating the aerogels at 120 °C for 24 h results in a significant increase in the wet integrity, even when the materials are exposed to agitation (Video S1, Supporting Information), most probably due to an increased permanent molecular contact between the nanoparticles. Hence, the treatment makes the AG^{nZIF-8} aerogels suitable for wet applications, which was demonstrated by using them as adsorbents for water purification.

A model experiment for water treatment based on the adsorption of the anionic dyes brilliant blue G (BB) and Congo red (CR) was set up at pH 7.4 with a dye concentration of 0.05 mg g^{-1} (Figure S12, Supporting Information). After soaking aerogel pieces (15–20 mg) in dye solutions for 336 h, an adsorption capacity of 48 ± 5 and 43 ± 4 mg g^{-1} for BB and CR, respectively, was established (Figure 2e). The insets in Figure 2e and the scanning electron microscopy (SEM) images in Figure 2f and Figure S13 (Supporting Information) show that the macrostructure and microstructure of the aerogels were preserved after the dye sorption, despite the extended treatment in water.

The dye molecules are relatively large: 1.4–1.7 nm for BB and 2.5 nm for CR, compared to the 1.2 nm pores of the MOFs that are separated by smaller windows of 0.36 nm.[27,28] The effective aperture of the cavity windows of ZIF-8 has been calculated to be ≈0.7 nm.[29] However, there are several studies where ZIF-8 has been observed to adsorb larger molecules than its pores.[30] This suggests that the adsorption occurs both on exterior surfaces of nZIF-8 particles and on CNFs, owing to charge exchange, and at least partially inside the pores (Table S7, Supporting Information). A first effort to separate the mechanisms behind the dye adsorption was to fit the data to pseudo-first-order and pseudo-second-order adsorption kinetics models (Figure S14 and Table S8, Supporting Information).[31] The results show a better fit for the second-order model, and hence better describe the adsorption kinetics as chemical adsorption. However, in order to identify the exact adsorption mechanisms,
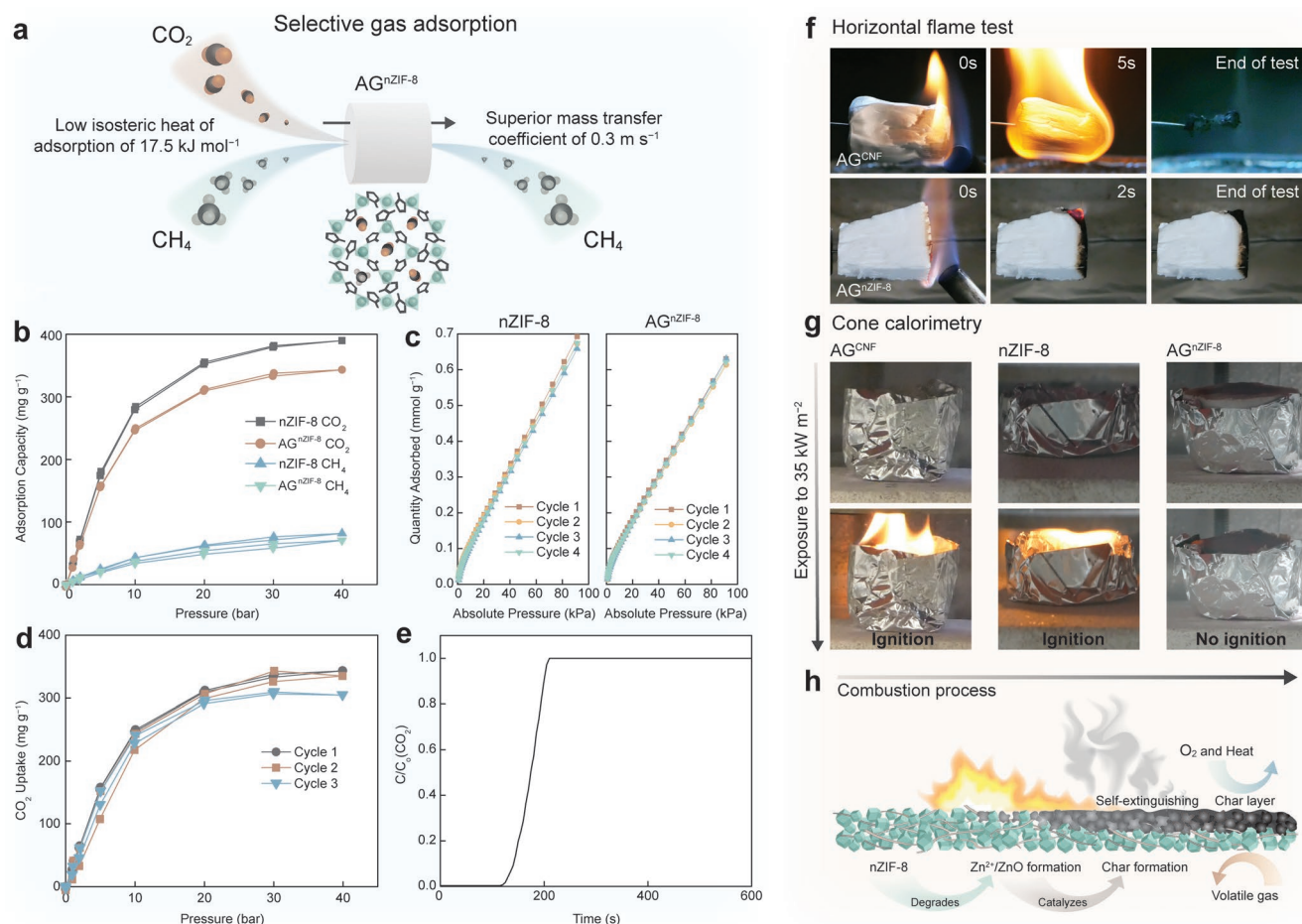
Figure 3. Gas adsorption and separation performance and flame-retardant properties. a) Schematic image of how the AG^{nZIF-8} aerogels selectively adsorb and hinder the transmission of CO_2 while allowing the passage of CH_4. b) Gravimetric equilibrium adsorption isotherms of CO_2 and CH_4 as a function of gas pressure at 293 K. c) Cyclic equilibrium CO_2 adsorption isotherms in pristine nZIF-8 powder and in AG^{nZIF-8} at 293 K. d) Cyclic equilibrium CO_2 adsorption isotherms in AG^{nZIF-8} at 293 K. e) CO_2 column breakthrough measurement of AG^{nZIF-8} at 293 K and 2 bars with a flow direction parallel to the direction of freezing. f) Horizontal flame burning test of pure CNF aerogels (AG^{CNF}) and AG^{nZIF-8}. The panels show photos of the samples at the start of the flame test, 2 or 5 s after flame removal, and the residues at the end of the test. g) Photographs of AG^{CNF}, nZIF-8, and AG^{nZIF-8} samples before the cone calorimetry test (top row) and after a heat flux exposure of 35 kW m^{-2} (bottom row). h) Proposed schematic mechanism[32] for the self-extinguishing behavior of the AG^{nZIF-8}.

further work is needed and the combination of experimental results and for example molecular dynamics simulations would be a fruitful continuation of the present work.

Our robust aerogels are valuable for other purification purposes, such as biogas upgrading and natural gas cleaning, for which the adsorption capacity must be high, reversible and specific to achieve a high enough separation (**Figure 3**a). Therefore, we measured the adsorption of CO_2 and CH_4 in AG^{nZIF-8} and compared it to a reference nZIF-8 MOF powder, at 293 K up to 40 bars (Figure 3b and Figure S15, Supporting Information). The CO_2 uptake was 343 and 390 mg g^{-1} for AG^{nZIF-8} and nZIF-8, respectively, while the corresponding CH_4 uptake capacity was only 71 and 82 mg g^{-1}, respectively. These results demonstrate a crucial property of the prepared aerogels: the adsorption capacity of the MOF particles in the aerogels is unaffected by the presence of the CNF network, and the adsorption can be specific to certain molecules. Compared with the nZIF-8 powder, the slightly decreased adsorption capacity of the aerogels (≈13%) is in proportion to the dry CNF content (10%)

and the decrease in the specific surface area of AG^{nZIF-8} aerogels (9%) (Table S4, Supporting Information). Based on this, it can be suggested that the higher CO_2 adsorption capacity, compared with that of CH_4, is due to the strong interactions between the CO_2 molecules and the ZIF-8 structure.[33] For a 50/50 (mol/mol) gas mixture at pressures relevant to biogas upgrading (i.e., 4 and 10 bars), the selectivity at equilibrium for AG^{nZIF-8}, calculated as CO_2:CH_4, was found to be 8:1. Thus, the selectivity for AG^{nZIF-8} is slightly higher than that for pure nZIF-8 powder, which has the corresponding selectivities of 6:1 for 4 bar and 7:1 for 10 bar. These selectivity values are highly competitive with other adsorbents used to separate CO_2 from CH_4, such as molecular sieves or zeolites.[34]

By measuring the adsorption isotherms of AG^{nZIF-8} at different temperatures (i.e., 0, 10, and 20 °C), it was possible to determine the isosteric heat release of adsorption for CO_2 to be 17.5 kJ mol^{-1} (Figures S16 and S17, Supporting Information). This value is similar to earlier reports for ZIF-8 powders,[35] but lower than those for zeolites and porous carbon.[36] The cyclic

**ADVANCED
SCIENCE NEWS**

www.advancedsciencenews.com

**ADVANCED
MATERIALS**

www.advmat.de

low-pressure adsorption–desorption of CO_2 for both AG^{nZIF-8} and nZIF-8 was also measured (Figure 3c and Figure S18, Supporting Information), which showed a stable and reversible CO_2 uptake along with efficient regeneration upon a simple pressure reduction (i.e., no heating needed). The low heat of adsorption and the ease of regeneration suggest that CO_2 is physisorbed in the aerogels, as no loss of capacity was observed after four cycles at low pressures, in contrast to the chemisorption of CO_2 in zeolites.[37] Furthermore, the high-pressure CO_2 adsorption–desorption cycles shown in Figure 3d indicate that the adsorption capacity is retained at high pressures and does not decrease with cycling, suggesting a maintained structural stability of the nZIF-8 particles within the aerogel structure.

The CO_2 column breakthrough curve for AG^{nZIF-8} was also measured (Figure 3e), where the AG^{nZIF8} particles were stacked such that the gas flow through the column was parallel to the pore direction. The CO_2 breakthrough from the AG^{nZIF-8} column after 120 s exhibits a sharp breakthrough front, suggesting that the structured AG^{nZIF-8} with aligned pores offers rapid mass-transfer kinetics to the sorption sites. The mass transfer coefficient (k) was calculated to be 0.3 m s^{-1} (Table S9, Supporting Information) by modeling the breakthrough data following previous work.[38] This value is similar to that of structured freeze-cast zeolite A monoliths ($k = 0.3$ m s^{-1}) with lamellar pores.[38,39] These results also indicate that, by forming a structured anisotropic material, the aerogels can be beneficially utilized for industrial gas adsorption and separation applications with very low pressure loss.

The thermal properties and flame-retardant behavior of the materials were also investigated. In particular, the thermal and thermo-oxidative stability of neat CNF aerogel (AG^{CNF}), nZIF-8 powder and AG^{nZIF-8} were measured under both nitrogen and air atmosphere using thermogravimetric analysis (TGA) (Figure S19, Supporting Information). AG^{nZIF-8} demonstrated independent decomposition pathways of the components. Its thermal stability was good up to 400 °C under both nitrogen and air environments, aligning with previously published data.[27]

Given the thermal and thermo-oxidative stability of the materials, it was important to determine whether additional flame-retardant characteristics were present by using flammability tests and cone calorimetry measurements. In the flammability tests, we exposed the samples to a flame, which showed that AG^{CNF} was easily ignited and that the flames rapidly spread through and consumed the entire sample (Figure 3f and Video S2, Supporting Information). In contrast, AG^{nZIF-8} showed exceptional flame-retardant properties. It prevented the flame from spreading and suppressed the flame only 3 s after ignition, thereby leaving a coherent residue accounting for 95 ± 2% of the initial weight (Figure 3f and Video S3, Supporting Information). The flame-retardant behavior was further investigated using oxygen-consumption cone calorimetry under a heat flux of 35 kW m^{-2}, which simulates the heat fluxes typically found in early-stage fire scenarios (Figure 3g; Figure S20 and Table S10, Supporting Information).[40] Upon exposure to heat flux, the neat AG^{CNF} aerogel quickly ignited, with a time to ignition of 12 ± 2 s, and burnt vigorously, with a peak heat-release rate of 102 ± 1 kW m^{-2}. During combustion, the structure collapsed, leaving a thin charred film as the final residue

with 5 ± 1% of the original mass. Neat nZIF-8 powder, which was evaluated as a reference sample, displayed a longer time to ignition of 33 ± 1 s, with a peak heat-release rate of 102 ± 7 kW m^{-2}—that is, similar to that of the CNFs—and a final residue accounting for 35 ± 3% of the starting weight. Surprisingly, AG^{nZIF-8} did not ignite at all, which is extremely rare for polymeric materials, probably because the released volatile gases did not reach the concentration required for ignition. On the other hand, due to the high temperatures and the presence of oxygen, the sample was partially consumed by smoldering—that is, solid-state oxidation in the absence of flame—leading to total smoke-release values of 47.1 ± 11.3 m^2 m^{-2}. This value is extremely low, especially in comparison with commercially available polymer foams, whose equivalent values normally range from 200 to 400 m^2 m^{-2}—that is, up to ten times greater than those of our MOF-based aerogels.[41]

The residues collected after cone calorimetry were further investigated using SEM, X-ray diffraction (XRD), and Raman spectroscopy analysis (Figures S21 and S22, Supporting Information). Compared with the AG^{CNF} and nZIF-8 powder, the AG^{nZIF-8} kept its original microstructure, with oriented pores and formed sub-micrometer particles on the cell walls comprised of zinc oxide (ZnO), as revealed by XRD (Figure S22, Supporting Information) and in accordance with TGA measurements in air (Figure S19, Supporting Information). The reasons behind the observed excellent flame-retardant properties can be explained based on the above findings and the recently discussed fire-retardancy mechanisms for MOF-containing aerogels.[32] As schematically depicted in Figure 3h, when the MOF-containing aerogel is exposed to a flame or a high heat flux, the insulating structure of the aerogel significantly limits the through-thickness heating rates and can hence favor char formation (of the CNFs).[42] Furthermore, the presence of nZIF-8 provides structural integrity at high temperatures and helps in preventing the collapse of the structure, thus further maintaining a favorable thermal gradient cross the material. The Zn^{2+} ions in the ZIF-8 also contribute by promoting the char formation from the CNFs and nZIF-8 particles. Hence, a limited number of combustible volatiles is released when the nanoMOF/CNF aerogels are exposed to a flame or an impinging heat flux, facilitating self-extinguishing and non-igniting behavior. In addition, during cone calorimetry, flame-induced combustion is replaced by thermo-oxidative processes that yield a charred residue composed of ZnO. The observed self-extinguishing and non-igniting behavior place the MOF-based aerogels among the best-performing aerogels, which include cellulose and high-aspect-ratio inorganic nanoparticles prepared via similar routes.[21,41,43] Moreover, the observed non-igniting behavior represents an excellent performance similar to that of phenolic resins, which are among the best commercially available fossil-based flame-retardant foams. The limited amount of smoke released would also impact safety, as the presence of smoke has been demonstrated to limit humans' ability to react and escape from a fire while also resulting in negative long-term health effects.[44] This further demonstrates the potential impact of the achieved flame retardancy.

The MOFs provide mechanical support to the aerogels during combustion, preventing them from collapsing and greatly preserving the original structure; moreover, there is a
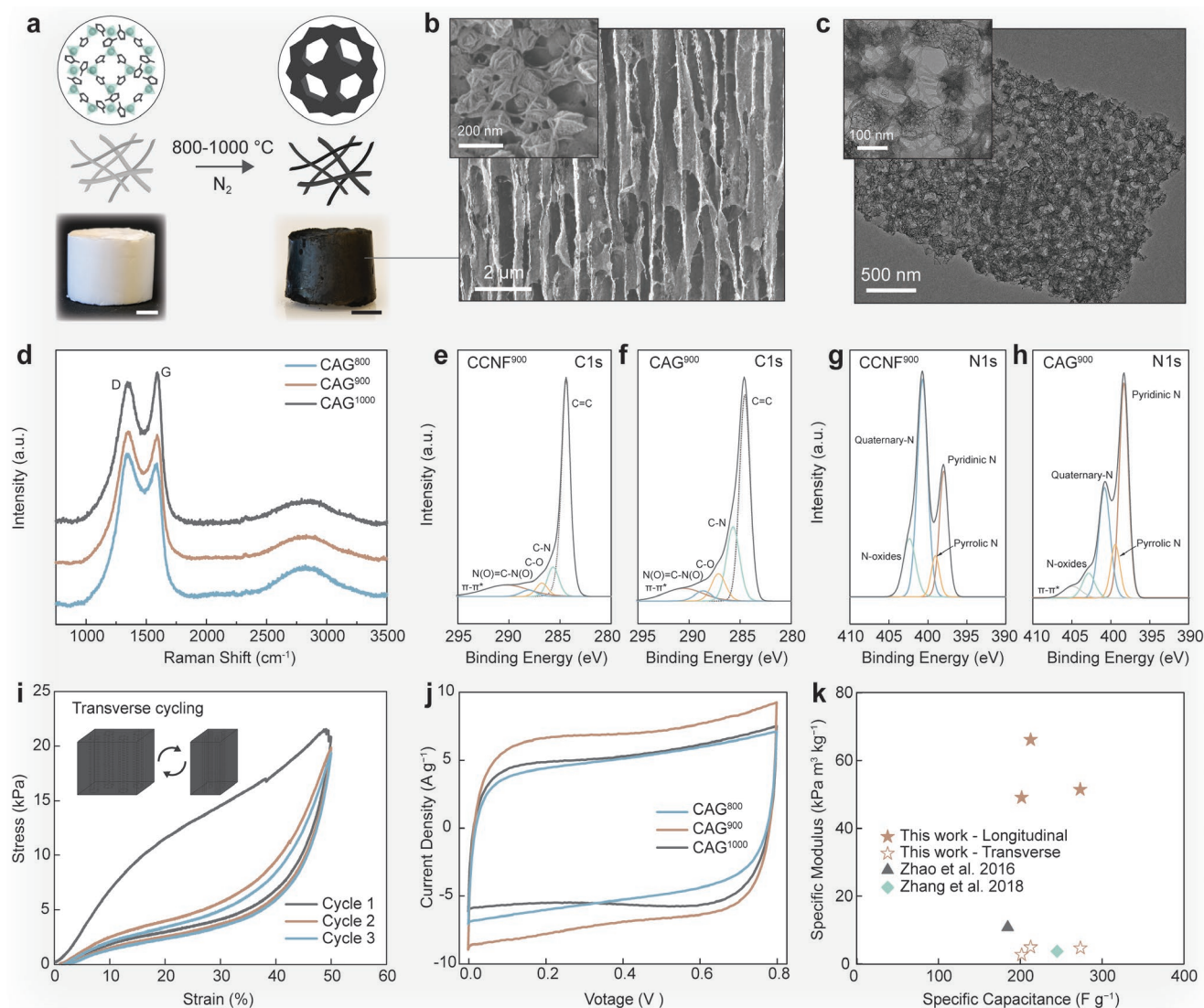
Figure 4. Carbonization characteristics and charge storage for the carbonized aerogels. a) Photographs and schematic drawings of non-carbonized and carbonized AG^{nZIF-8} aerogels (CAGs) at 900 °C (CAG^{900}). Scale bars: 5 mm. b) SEM and c) transmission electron microscopy (TEM) images of CAG^{900}. d) Raman spectra of AG^{nZIF-8} carbonized at 800 (CAG^{800}), 900 (CAG^{900}), and 1000 (CAG^{1000}) °C. e,f) XPS C1s spectra of AG^{CNF} (e) carbonized at 900 °C (CCNF^{900}) and CAG^{900} (f), as well as g,h) N1s spectra of CCNF^{900} (g) and CAG^{900} (h). i) Cyclic compressive testing (three cycles) to 50% compression of the original size of a CAG^{900}. j) Cyclic voltammetry curves of CAGs at a scan rate of 50 mV s^{-1} and k) Ashby plot of the specific modulus (transverse and longitudinal) and specific capacitance of CAGs at 800, 900, and 1000 °C, compared with those of other reported conductive aerogel electrodes.[45]

high nitrogen content in the chemical composition of nZIF-8 and CNFs. Thus, we were able to develop self-supporting N-doped carbon aerogels. Interestingly, and somewhat surprisingly, the carbonized AG^{nZIF-8} aerogels (CAGs) had the same exterior architecture as the non-carbonized AG^{nZIF-8} aerogels (**Figure 4**a). In contrast, a carbonized AG^{CNF} at 900 °C (CCNF^{900}) collapsed into small, fragmented and compressed carbonized pieces. The microstructure was also preserved in the CAGs, in which the nZIF-8 particles were converted into carbon nanocages aligned by the carbon nanofibrils derived from the CNFs (Figure 4b,c, and Figures S23–S26, Supporting Information).

Carbonization temperatures of 800–1000 °C were used (i.e., CAG^{800}, CAG^{900}, and CAG^{1000}) to tune the degree of

graphitization and the physicochemical properties of the CAGs (Figures S27 and S28 and Table S11, Supporting Information). CAG^{1000} showed the highest intensity ratio between the G and D bands ($I_G/I_D = 1.05$) from Raman spectra (Figure 4d)—a ratio correlated to the degree of graphitic ordering. This finding is consistent with the corresponding X-ray photoelectron spectroscopy (XPS) C1s spectra, which indicated a 41%–51% sp^2 carbon structure in the CAGs (Figure 4e,f; Figure S28 and Table S12, Supporting Information). These results indicate that the fraction of graphitic domains in the CAGs increases with increasing carbonization temperature. The degree of N-doping of the carbonized samples was tuned by combining the incorporation of MOFs (Figure 4g,h) with an increase in carbonization temperature (Figure S28 and Table S11, Supporting Information). The

results show that MOFs improved the N-doping content in the CAGs by up to 10–15 at%, compared with 1 at% for CCNF^{900} (Table S13, Supporting Information). Even after carbonization, the aerogels maintained an astonishing level of mechanical integrity and could be compressed in both the longitudinal and transverse directions, with a specific compressive modulus of 50–70 and 3–5 kPa m^3 kg^{-1}, respectively (Figure S29 and Table S14, Supporting Information). The CAGs also showed an excellent shape recovery of close to 100% for all three cycles after 50% compression in the transverse direction (Figure 4i and Figure S30, Supporting Information).

Thanks to these aerogels with robust mechanical integrity, high specific surface areas (700–1100 m^2 g^{-1}) (Figures S31 and S32 and Table S15, Supporting Information), and high N-doping, it was possible to evaluate the energy-storage ability of the carbonized MOF aerogels as structural electrodes in a symmetrical two-electrode supercapacitor system. CAG^{900} exhibited the highest capacitance (273 F g^{-1} at 50 mV s^{-1}) (Figure 4j), high stability with a 98.3% capacitance retention after 20 000 charge/discharge cycles (Figure S33, Supporting Information), and high rate performance of 75% at 50 A g^{-1} coupled with an energy density of 7.42 Wh kg^{-1} at a power density of 15.6 kW kg^{-1} (Figure S34, Supporting Information). This is presumably due to the synergetic trade-off between high nitrogen doping and a high specific surface area (970 m^2 g^{-1}). More interestingly, their unique combination of mechanical compressive stiffness and energy storage places the CAGs comparable with the best structural aerogel electrodes reported to date (Figure 4k).[45] The results show the promising potential of carbonized MOF-based aerogels for use in structural energy-storage devices.

3. Conclusion

We have demonstrated a simple water-based procedure for fabricating multifunctional MOF-based aerogels containing 90 wt% nanoMOF particles. The high MOF content was achieved by combining colloidal-quality nanoMOF particles with high-aspect-ratio CNFs that were freeze-cast and lyophilized. The unique characteristics of the significantly longer and more slender CNFs are superior to typical CNFs in creating an entangled gel network at very low concentrations, making them ideal as a substrate for MOF particles. Hence, the combination of these two components resulted in highly porous anisotropic aerogels that were mechanically robust, shape-recoverable in the dry state, and wet-stable, without any added crosslinking agent. The unique mechanical integrity of these aerogels was maintained even after the carbonization step that yielded N-doped carbon aerogels. The versatile use of these aerogels was then demonstrated, revealing them to be effective for water purification, gas storage and separation, flame retardancy, and supercapacitors. Given the simple fabrication process and the demonstrated applications, we conclude that these MOF-based aerogels (non-carbonized and carbonized) are potential breakthrough materials in several applications. The next steps will be to scale up the fabrication to make larger coherent materials and demonstrate their versatility by incorporating other types of MOFs designed for specific applications. The further development of these aerogels will pave the way for advanced lightweight nanomaterials with potential applications in fields requiring fire safety, pollution removal, and energy-storage capabilities.

Conflict of Interest

The authors declare no conflict of interest.

Data Availability Statement

The data that support the findings of this study are available from the corresponding author upon reasonable request.

[1] a) R. Freund, U. Lächelt, T. Gruber, B. Rühle, S. Wuttke, *ACS Nano* **2018**, *12*, 2094; b) G. Yilmaz, S. B. Peh, D. Zhao, G. W. Ho, *Adv. Sci.* **2019**, *6*, 1901129; c) O. M. Yaghi, *J. Am. Chem. Soc.* **2016**, *138*, 15507; d) R. B. Lin, S. Xiang, B. Li, Y. Cui, W. Zhou, G. Qian, B. Chen, *Isr. J. Chem.* **2018**, *58*, 949.

[2] A. Ejsmont, J. Andreo, A. Lanza, A. Galarda, L. Macreadie, S. Wuttke, S. Canossa, E. Ploetz, J. Goscianska, *Coord. Chem. Rev.* **2021**, *430*, 213655.

**ADVANCED
SCIENCE NEWS**

www.advancedsciencenews.com

**ADVANCED
MATERIALS**

www.advmat.de

[3] Z. Ji, H. Wang, S. Canossa, S. Wuttke, O. M. Yaghi, *Adv. Funct. Mater.* **2020**, *30*, 2000238.

[4] M. Kalaj, K. C. Bentz, S. Ayala, Jr., J. M. Palomba, K. S. Barcus, Y. Katayama, S. M. Cohen, *Chem. Rev.* **2020**, *120*, 8267.

[5] a) L. Li, S. Xiang, S. Cao, J. Zhang, G. Ouyang, L. Chen, C.-Y. Su, *Nat. Commun.* **2013**, *4*, 1774; b) C. Duan, Y. Yu, J. Li, L. Li, B. Huang, D. Chen, H. Xi, *Sci. China Mater.* **2021**, *64*, 1305.

[6] H. Wang, B. H. Chen, D. J. Liu, *Adv. Mater.* **2021**, *33*, 2008023.

[7] B. Zhang, J. Zhang, C. Liu, L. Peng, X. Sang, B. Han, X. Ma, T. Luo, X. Tan, G. Yang, *Sci. Rep.* **2016**, *6*, 21401.

[8] L. Zhu, L. Zong, X. Wu, M. Li, H. Wang, J. You, C. Li, *ACS Nano* **2018**, *12*, 4462.

[9] a) S. Zhou, V. Apostolopoulou-Kalkavoura, M. V. T. da Costa, L. Bergström, M. Strømme, C. Xu, *Nano-Micro Lett.* **2020**, *12*, 1; b) M. Jiang, H. Li, L. Zhou, R. Xing, J. Zhang, *ACS Appl. Mater. Interfaces* **2018**, *10*, 827.

[10] M. L. Pinto, S. Dias, J. Pires, *ACS Appl. Mater. Interfaces* **2013**, *5*, 2360.

[11] a) P. Hou, G. Xing, D. Han, H. Wang, C. Yu, Y. Li, *J. Solid State Chem.* **2018**, *265*, 184; b) Y. Yang, Y.-X. Liu, Y. Li, B.-W. Deng, B. Yin, M.-B. Yang, *J. Mater. Chem. A* **2020**, *8*, 17257; c) L. Valencia, H. N. Abdelhamid, *Carbohydr. Polym.* **2019**, *213*, 338; d) S. Alwin, V. Ramasubbu, X. S. Shajan, *Bull. Mater. Sci.* **2018**, *41*, 27; e) V. Ramasubbu, S. Alwin, E. Mothi, X. S. Shajan, *Mater. Lett.* **2017**, *197*, 236; f) P. Cheng, M. Kim, H. Lim, J. Lin, N. L. Torad, X. Zhang, M. S. A. Hossain, C. W. Wu, C. Wang, J. Na, *Adv. Sustainable Syst.* **2020**, *4*, 2000060; g) J. Y. Seo, Y. Song, J.-H. Lee, H. Kim, S. Cho, K.-Y. Baek, *ACS Appl. Mater. Interfaces* **2021**, *13*, 33516; h) N. Huang, H. Drake, J. Li, J. Pang, Y. Wang, S. Yuan, Q. Wang, P. Cai, J. Qin, H. C. Zhou, *Angew. Chem.* **2018**, *130*, 9054; i) J. Qu, D. Chen, N. Li, Q. Xu, H. Li, J. He, J. Lu, *Small* **2018**, *14*, 1800343.

[12] H. Zhu, X. Yang, E. D. Cranston, S. Zhu, *Adv. Mater.* **2016**, *28*, 7652.

[13] J. Rostami, K. Gordeyeva, T. Benselfelt, E. Lahchaichi, S. A. Hall, A. V. Riazanova, P. A. Larsson, G. C. Ciftci, L. Wågberg, *Mater. Today* **2021**.

[14] a) C. Lei, J. Gao, W. Ren, Y. Xie, S. Y. H. Abdalkarim, S. Wang, Q. Ni, J. Yao, *Carbohydr. Polym.* **2019**, *205*, 35; b) H. N. Abdelhamid, A. P. Mathew, *Coord. Chem. Rev.* **2022**, *451*, 214263.

[15] a) L. Wang, H. Xu, J. Gao, J. Yao, Q. Zhang, *Coord. Chem. Rev.* **2019**, *398*, 213016; b) R. M. Rego, G. Kuriya, M. D. Kurkuri, M. Kigga, *J. Hazard. Mater.* **2021**, *403*, 123605.

[16] Z. Inonu, S. Keskin, C. Erkey, *ACS Appl. Nano Mater.* **2018**, *1*, 5959.

[17] C. Avci, I. Imaz, A. Carné-Sánchez, J. A. Pariente, N. Tasios, J. Pérez-Carvajal, M. I. Alonso, A. Blanco, M. Dijkstra, C. López, *Nat. Chem.* **2018**, *10*, 78.

[18] M. Nordenström, A. Fall, G. Nyström, L. Wågberg, *Langmuir* **2017**, *33*, 9772.

[19] L. Geng, N. Mittal, C. Zhan, F. Ansari, P. R. Sharma, X. Peng, B. S. Hsiao, L. D. Söderberg, *Macromolecules* **2018**, *51*, 1498.

[20] a) H. Nabipour, S. Nie, X. Wang, L. Song, Y. Hu, *Composites, Part A* **2020**, *129*, 105720; b) J. Mao, M. Ge, J. Huang, Y. Lai, C. Lin, K. Zhang, K. Meng, Y. Tang, *J. Mater. Chem. A* **2017**, *5*, 11873.

[21] B. Wicklein, A. Kocjan, G. Salazar-Alvarez, F. Carosio, G. Camino, M. Antonietti, L. Bergström, *Nat. Nanotechnol.* **2015**, *10*, 277.

[22] F. Rezaei, P. Webley, *Sep. Purif. Technol.* **2010**, *70*, 243.

[23] M. F. Ashby, R. Medalist, *Metall. Trans. A* **1983**, *14*, 1755.

[24] a) A. A. Tiba, A. V. Tivanski, L. R. MacGillivray, *Nano Lett.* **2019**, *19*, 6140; b) N. Buchtová, C. Pradille, J.-L. Bouvard, T. Budtova,

Soft Matter **2019**, *15*, 7901; c) T. Nishino, K. Takano, K. Nakamae, *J. Polym. Sci., Part B: Polym. Phys.* **1995**, *33*, 1647.

[25] a) W. Yang, J. McKittrick, *Acta Biomater.* **2013**, *9*, 9065; b) W. Yang, C. Chao, J. McKittrick, *Acta Biomater.* **2013**, *9*, 5297.

[26] G. Laivins, A. Scallan, *Prod. Papermaking* **1993**, *2*, 1235.

[27] K. S. Park, Z. Ni, A. P. Côté, J. Y. Choi, R. Huang, F. J. Uribe-Romo, H. K. Chae, M. O'Keeffe, O. M. Yaghi, *Proc. Natl. Acad. Sci. USA* **2006**, *103*, 10186.

[28] D. M. Polyukhov, A. S. Poryvaev, S. A. Gromilov, M. V. Fedin, *Nano Lett.* **2019**, *19*, 6506.

[29] D. M. Polyukhov, A. S. Poryvaev, A. S. Sukhikh, S. A. Gromilov, M. V. Fedin, *ACS Appl. Mater. Interfaces* **2021**, *13*, 40830.

[30] D. Fairen-Jimenez, S. Moggach, M. Wharmby, P. Wright, S. Parsons, T. Duren, *J. Am. Chem. Soc.* **2011**, *133*, 8900.

[31] L. Mo, H. Pang, Y. Tan, S. Zhang, J. Li, *Chem. Eng. J.* **2019**, *378*, 122157.

[32] H. Nabipour, S. Nie, X. Wang, L. Song, Y. Hu, *Cellulose* **2020**, *27*, 2237.

[33] a) H. Hayashi, A. P. Côté, H. Furukawa, M. O'Keeffe, O. M. Yaghi, *Nat. Mater.* **2007**, *6*, 501; b) S. K. Nune, P. K. Thallapally, A. Dohnalkova, C. Wang, J. Liu, G. J. Exarhos, *Chem. Commun.* **2010**, *46*, 4878.

[34] a) H. Yi, F. Li, P. Ning, X. Tang, J. Peng, Y. Li, H. Deng, *Chem. Eng. J.* **2013**, *215*, 635; b) T. Ariyanto, K. Masruroh, G. Y. S. Pambayun, N. I. F. Mukti, R. B. Cahyono, A. Prasetya, I. Prasetyo, *ACS Omega* **2021**, *6*, 19194; c) M. Mofarahi, F. Gholipour, *Microporous Mesoporous Mater.* **2014**, *200*, 1.

[35] G. Autié Castro, E. de Oliveira Jardim, E. Reguera, E. Vilarrasa-García, E. Rodríguez-Castellón, C. L. Cavalcante Jr., *Biol. Chem. Res.* **2017**, *4*, 324.

[36] a) K. N. Son, G. E. Cmarik, J. C. Knox, J. A. Weibel, S. V. Garimella, *J. Chem. Eng. Data* **2018**, *63*, 1663; b) M. D. Hornbostel, J. Bao, G. Krishnan, A. Nagar, I. Jayaweera, T. Kobayashi, A. Sanjurjo, J. Sweeney, D. Carruthers, M. A. Petruska, *Carbon* **2013**, *56*, 77.

[37] a) F. Akhtar, Q. Liu, N. Hedin, L. Bergström, *Energy Environ. Sci.* **2012**, *5*, 7664; b) F. Akhtar, L. Andersson, N. Keshavarzi, L. Bergström, *Appl. Energy* **2012**, *97*, 289.

[38] a) W. Zhang, K. Narang, S. B. Simonsen, M. Gudik-Sørensen, L. Han, F. Akhtar, A. Kaiser, *Energy Technol.* **2020**, *8*, 1900781; b) A. Ojuva, M. Järveläinen, M. Bauer, L. Keskinen, M. Valkonen, F. Akhtar, E. Levänen, L. Bergström, *J. Eur. Ceram. Soc.* **2015**, *35*, 2607.

[39] K. Narang, K. Fodor, A. Kaiser, F. Akhtar, *RSC Adv.* **2018**, *8*, 37277.

[40] B. Schartel, T. Hull, *Fire Mater.* **2007**, *31*, 327.

[41] F. Carosio, L. Medina, J. Kochumalayil, L. A. Berglund, *Adv. Mater. Interfaces* **2021**, *8*, 2101111.

[42] J. Alongi, G. Camino, G. Malucelli, *Carbohydr. Polym.* **2013**, *92*, 1327.

[43] H.-B. Chen, D. A. Schiraldi, *Polym. Rev.* **2019**, *59*, 1.

[44] a) R. G. Gann, *Fire Technol.* **2004**, *40*, 201; b) J. Giebułtowicz, M. Rużycka, P. Wroczyński, D. A. Purser, A. A. Stec, *Forensic Sci. Int.* **2017**, *277*, 77.

[45] a) H.-B. Zhao, L. Yuan, Z.-B. Fu, C.-Y. Wang, X. Yang, J.-Y. Zhu, J. Qu, H.-B. Chen, D. A. Schiraldi, *ACS Appl. Mater. Interfaces* **2016**, *8*, 9917; b) E. Zhang, W. Liu, X. Liu, Z. Zhao, Y. Yang, *Mater. Today Commun.* **2020**, *24*, 101125; c) Q. Zhang, Y. Wang, B. Zhang, K. Zhao, P. He, B. Huang, *Carbon* **2018**, *127*, 449.